

# GaN nanowire coated with atomic layer deposition of tungsten: a probe for near-field scanning microwave microscopy

Joel C Weber<sup>1,2</sup>, Paul T Blanchard<sup>1</sup>, Aric W Sanders<sup>1</sup>, Jonas C Gertsch<sup>2</sup>, Steven M George<sup>2</sup>, Samuel Berweger<sup>1</sup>, Atif Imtiaz<sup>1</sup>, Kevin J Coakley<sup>1</sup>, Thomas M Wallis<sup>1</sup>, Kris A Bertness<sup>1</sup>, Pavel Kabos<sup>1</sup>, Norman A Sanford<sup>1</sup> and Victor M Bright<sup>2</sup>

<sup>1</sup>National Institute of Standards and Technology, Boulder, CO 80305, USA

<sup>2</sup>University of Colorado at Boulder, Boulder, CO 80309, USA

E-mail: [Joel.Weber@colorado.edu](mailto:Joel.Weber@colorado.edu) and [Joel.Weber@nist.gov](mailto:Joel.Weber@nist.gov)

Received 5 June 2014, revised 29 July 2014

Accepted for publication 12 August 2014

Published 26 September 2014

## Abstract

GaN nanowires were coated with tungsten by means of atomic layer deposition. These structures were then adapted as probe tips for near-field scanning microwave microscopy. These probes displayed a capacitive resolution of  $\sim 0.03$  fF, which surpasses that of a commercial Pt tip. Upon imaging of MoS<sub>2</sub> sheets with both the Pt and GaN nanowire tips, we found that the nanowire tips were comparatively immune to surface contamination and far more durable than their Pt counterparts.

Keywords: atomic layer deposition, gallium nitride, molybdenum disulphide, nanowires, scanning microwave microscopy, tungsten

(Some figures may appear in colour only in the online journal)

## Introduction

The need to better characterize advanced materials at the nanoscale has precipitated the development of a multitude of scanning-probe instruments. Since resolution and repeatability generally depend upon both the probe's dimensions and material properties, careful attention to its design is essential for advancing state-of-the-art imaging. The advent of well-controlled nanostructures, including nanoparticles, nanotubes, and nanowires, provides new opportunities for realizing probes capable of exploiting their unique architecture in order to obtain enhanced measurement capabilities. While modified AFM probes were initially dominated by carbon nanotube-based atomic force microscopy tips [1–3], new research has expanded their applications to tip-enhanced Raman spectroscopy [4], scanning tunneling microscopy [5], near-field optical microscopy [6], and scanning electrochemical microscopy (SEM) [7], among many others. In this paper, we present a tungsten (W) atomic layer deposition (ALD) NW-based probe well suited for near-field scanning

microwave microscopy (NSMM). The probe's robust, high-aspect ratio design makes it an ideal platform for use in alternative scanning-probe microscopes.

NSMM provides a non-destructive technique for studying nanoscale-properties for a variety of materials [8–14]. Its broadband illumination extends device characterization into the gigahertz range, complementing scanning capacitance and scanning impedance microscopy. Tracking changes in evanescent fields at the tip-sample interface, typically as a change in the microwave reflection coefficient  $S_{11}$ , enables simultaneous mapping of topography, conductivity, and permittivity [15–20]. Recent work emphasizes improved quantitative analysis of NSMM through the use of calibration standards. This approach enables the conversion of the measured  $S_{11}$  signal into the complex impedance plane and the separation of conductance and capacitance contributions [21–27]. Reliable calibrations require an understanding of the effective electromagnetic probe radius during scanning in addition to knowledge of the device under study [28, 29]. While this can be assessed through a variety of means

**Table 1.** ALD surface reactions for buffer, microwave pathway, and capping layers.

Al <sub>2</sub> O <sub>3</sub>	A	AlOH(see footnote 3) + Al(CH <sub>3</sub> ) <sub>3</sub> → AlOAl(CH <sub>3</sub> ) <sub>2</sub> (see footnote 3) + CH <sub>4</sub>
	B	AlCH <sub>3</sub> (see footnote 3) + H <sub>2</sub> O → AlOH(see footnote 3) + CH <sub>4</sub>
W	A	WF <sub>5</sub> (see footnote 3) + Si <sub>2</sub> H <sub>6</sub> → WSiF <sub>2</sub> H(see footnote 3) + SiF <sub>3</sub> H + 2H <sub>2</sub>
	B	WSiF <sub>2</sub> H(see footnote 3) + WF <sub>6</sub> → WWF <sub>5</sub> (see footnote 3) + SiF <sub>3</sub> H

including measuring capacitive approach curves, contact scanning-induced wear may alter probe dimensions thus necessitating an updated calibration between imaging runs.

We reported on the fabrication of a GaN NW probe exhibiting improved mechanical wear-resistance and comparable microwave sensitivity to a widely used commercial Pt tip [30]. Here, by significantly improving the microwave pathway with a W film through ALD, we have increased the capacitive resolution over an order of magnitude from ~0.7 fF to ~0.03 fF. Owing to the conformal nature of ALD with respect to the evaporative metal coating used previously, the effective tip diameter was reduced by ~60 nm, resulting in increased microwave and topographical spatial resolution. These improvements are further detailed through imaging of 2D MoS<sub>2</sub> sheets on a SiO<sub>2</sub> substrate. Here, the NW probe's high-aspect ratio and flexible structure appeared to reduce its sensitivity to surface contamination, yielding improved scanning contrast.

## Experimental method

The NSMM used to conduct these scans consists of an Agilent 5400<sup>3</sup> atomic force microscope (AFM) that incorporates a vector network analyzer (VNA) to source and receive microwave signals in the 1–20 GHz range. An integrated phase shifter improves broadband sensitivity by matching sample and transmission line (50 Ω) impedance with the complete microwave circuit described in detail elsewhere [22, 31]. The GaN NWs used for the fabrication of this probe were grown through catalyst-free molecular-beam epitaxy on a Si <111> substrate with an AlN buffer layer [32–34]. The NWs form a wurtzite crystalline structure and are essentially defect-free owing to their high-temperature, ultra-high-vacuum growth environment. A similar fabrication process, previously established in [27], was used to manufacture the probe. As before, a tipless Si cantilever (12 kHz CLR-10 tip by VISTAprobes) (see footnote 3) was used for the probe's foundation. To create a microwave pathway from the AFM chip body to the tip, the entire structure was coated using ALD with a structure comprised of 30 cycles Al<sub>2</sub>O<sub>3</sub> (3.5 nm)/63 cycles W (25.6 nm)/10 cycles Al<sub>2</sub>O<sub>3</sub> (1.2 nm) [35–37]. The depositions were conducted in a viscous flow stainless steel ALD reactor with an inner diameter of ~23 cm. The reactor body walls were kept constant at 130 °C while the precursor vessels were held at room temperature. N<sub>2</sub> was used as the

<sup>3</sup> Certain commercial equipment, instruments, or materials are identified in this paper in order to adequately specify the experimental procedure. Such identification implies neither recommendation nor endorsement by NIST, nor does it imply that the materials used are necessarily the best for the purpose.

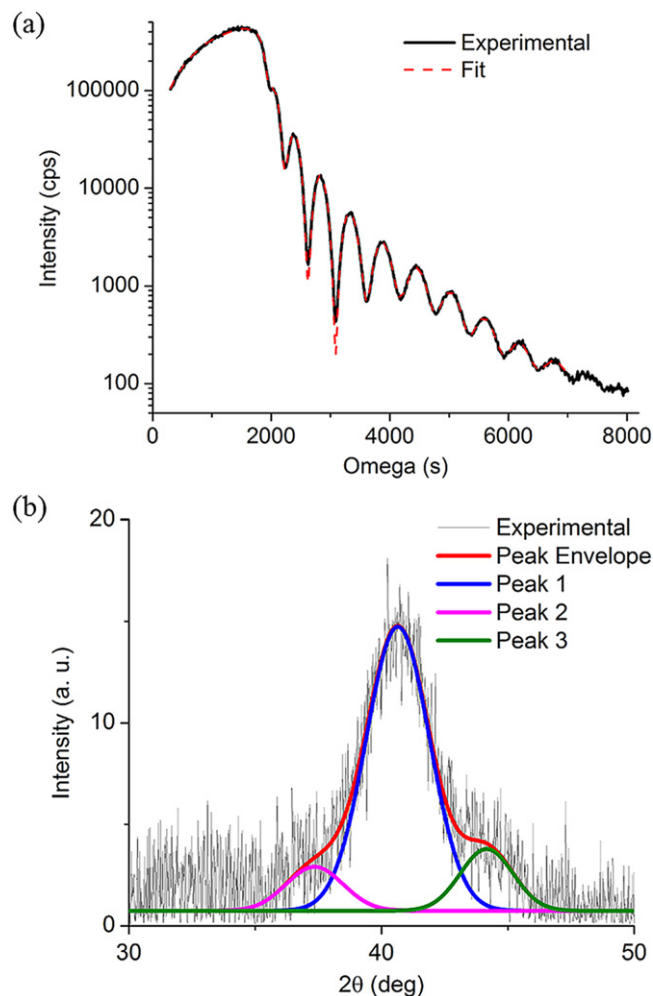


**Figure 1.** (a) XRR experimental data was used to independently determine the ALD thicknesses. The buffer Al<sub>2</sub>O<sub>3</sub> layer is 3.5 nm, the W layer is 25.6 nm, and the capping Al<sub>2</sub>O<sub>3</sub> layer is 1.2 nm. (b) XRD experimental results along with fitted peaks. The presence of a sharp center peak as well as a total of three peaks between 30° and 50° indicates the presence of mostly β-phase W. The three peaks are shifted slightly from the calculated peak positions of 34.3°, 39.6°, and 43.6°, indicating the presence of stress in the film [39].

carrier gas, with each precursor line having a flow of 40 sccm. Surface reactions for Al<sub>2</sub>O<sub>3</sub> and W are provided in table 1. Deposited thicknesses were independently measured through x-ray reflectivity (XRR) (figure 1(a)), while x-ray diffraction (XRD) data indicated the deposited metal to be comprised primarily of β-phase W [38] (figure 1(b)). Figure 2(a) is an SEM image showing the NW probe, post-ALD. The NW protrudes ~5 μm from the Si base and has a radius of ~120 nm. The uniform coverage afforded by ALD enables a

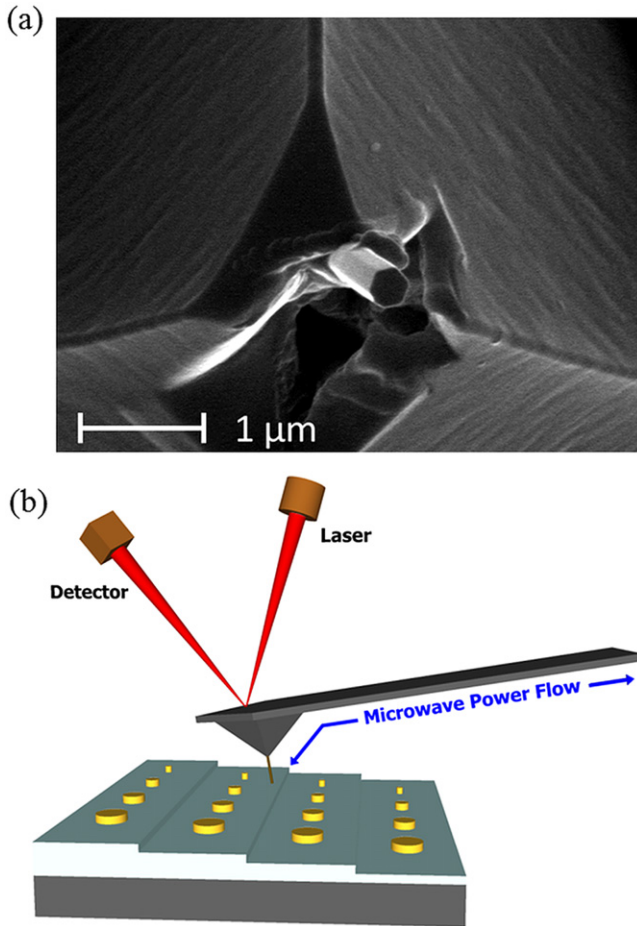


**Figure 2.** (a) SEM image of fabricated GaN NW probe post W ALD. (b) Illustration of microcapacitor calibration sample with 1–4  $\mu\text{m}$  diameter Au microcapacitors on 10 nm  $\text{SiO}_2$  steps with a silicon substrate.

continuous electrical pathway free of pinholes and cracks without significantly increasing the mechanical probe radius during scanning.

## Results and discussion

A microcapacitor sample presented in detail previously was used to calibrate the capacitance resolution of the ALD NW probe [22] (figure 2(b)). The sample consists of a silicon substrate with four  $10 \pm 0.3$  nm  $\text{SiO}_2$  steps ranging in thickness from 10 nm to 40 nm. Each  $\text{SiO}_2$  step is patterned with four circular metal pads comprised of 20 nm Ti/200 nm Au with diameters of 1  $\mu\text{m}$ –4  $\mu\text{m}$ . Prior to scanning, the W-ALD NW probe was brought into contact over the 40 nm thick  $\text{SiO}_2$  step, and the resonance peak was tuned to  $-50$  dBm at a frequency of 2.3 GHz. The VNA measuring frequency was offset from the minimum and held fixed during a  $50 \mu\text{m} \times 50 \mu\text{m}$  scan. In figure 3(a), the improved microwave contrast of the W-ALD NW probe can be clearly seen relative to the original Ti/Al NW probe (figure 3(b)). The difference in microwave signal, or  $|\Delta S_{11}|$ , between each Au microcapacitor pad and the surrounding  $\text{SiO}_2$  step on which the pad

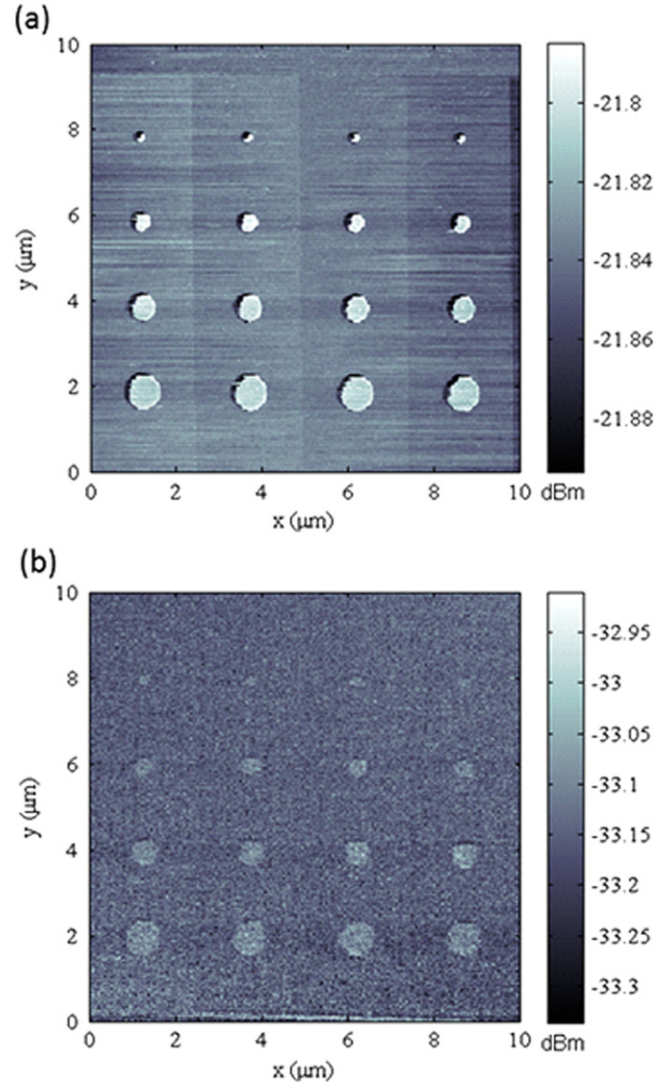


**Figure 3.** (a) Microwave reflection coefficient  $S_{11}$  image taken with the W-ALD NW probe (tip radius of  $\sim 150$  nm reported in [27]) showing contrast for both the microcapacitors and  $\text{SiO}_2$  steps. (b)  $S_{11}$  image taken with the Ti/Al.  $\text{SiO}_2$  steps are not visible while microcapacitor edge resolution is reduced. Both images were recorded at 2.3 GHz with VNA power set to 5 dBm and a scan speed of  $0.3 \text{ ln s}^{-1}$ .

was recorded.  $S_{11}$  is given by

$$S_{11} = \frac{Z_L - Z_0}{Z_L + Z_0}, \quad (1)$$

with  $Z_L$  being the load impedance and  $Z_0$  being the source impedance (transmission line impedance with a value of  $50 \Omega$ ).  $\Delta S_{11}$  thus measures a change in  $S_{11}$  and consequently the change in  $Z_L$  as the probe passes from a  $\text{SiO}_2$  region to a metal pad. Following [12], the  $|\Delta S_{11}|$  data were then converted to capacitance using the relation  $C_{\text{tot}} = \alpha^* |\Delta S_{11}|$  and fitted with a circuit model. The model consists of stray capacitance caused by the cantilever  $C_{\text{cant}}$  in parallel with three additional capacitances in series: tip capacitance  $C_{\text{tip}}$  due to the 12 nm  $\text{Al}_2\text{O}_3$  ALD passivation layer, dielectric capacitance  $C_{\text{diel}}$  from the  $\text{SiO}_2$  layer under the microcapacitor, and back or parasitic

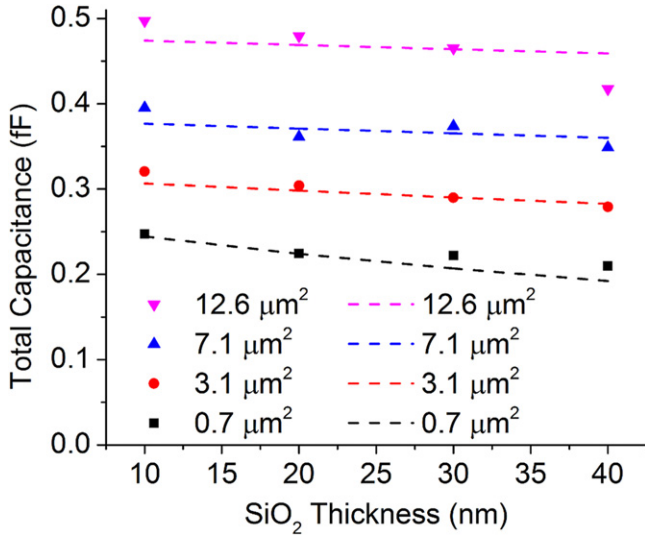


**Figure 4.**  $|\Delta S_{11}|$  between each microcapacitor and background  $\text{SiO}_2$  converted to capacitance and plotted as a function of  $\text{SiO}_2$  thickness (solid symbols). Experimental data for  $3.1 \mu\text{m}^2$  microcapacitors was fitted (dashed lines) using  $C_{\text{back}}$  and  $\alpha$  as fitting parameters. These parameters were then held constant for the other three microcapacitor areas shown.

capacitance  $C_{\text{back}}$  due to fringing effects and depletion in the silicon substrate. Because  $|\Delta S_{11}|$  data are presented as a difference measurement, effects caused by the largely constant  $C_{\text{cant}}$  may be ignored.  $C_{\text{back}}$  is treated as a fitting parameter that scales relative to the area of the microcapacitor in question with values on the order of 0.3 fF.  $C_{\text{tip}}$  and  $C_{\text{diel}}$  are modeled as simple parallel-plate capacitors governed by

$$C_{\text{tip}} = \frac{\epsilon_{\text{tip}} A_{\text{tip}}}{t_{\text{tip}}};$$

$$C_{\text{diel}} = \frac{\epsilon_{\text{diel}} A_{\text{diel}}}{t_{\text{diel}}};$$

$$\frac{1}{C_{\text{tot}}} = \frac{1}{C_{\text{tip}}} + \frac{1}{C_{\text{diel}}} + \frac{1}{C_{\text{back}}},$$

where  $A_{\text{tip}}$  is the area of the NW surface,  $A_{\text{diel}}$  is the area of the microcapacitor,  $t_{\text{tip}}$  is the thickness of the outer  $\text{Al}_2\text{O}_3$  ALD layer,  $t_{\text{diel}}$  is the thickness of the  $\text{SiO}_2$  layer,  $\epsilon_{\text{tip}}$  is the permittivity of  $\text{Al}_2\text{O}_3$ , and  $\epsilon_{\text{diel}}$  is the permittivity of  $\text{SiO}_2$ . To obtain the plot shown in figure 4, the model was fitted to the experimental data for the  $3.1 \mu\text{m}^2$  microcapacitors with  $\alpha = 0.5 \text{ fF}/\Delta\text{dBm}$ . The  $\alpha$  and  $C_{\text{back}}$  fitting parameters were held constant and applied to the other three microcapacitor sizes. As expected, increasing microcapacitor area and decreasing dielectric thickness correlate with an increase in measured total capacitance. The capacitance model tracks these trends well with deviations likely attributed to error caused by fringe effects in the parallel-plate capacitors and a variable  $C_{\text{tip}}$  due to bending of the NW during scanning.

To determine the resolution limit and measurement noise floor attributed to the W-ALD NW probe and microscope, a line scan across the  $\text{SiO}_2$  steps without the presence of microcapacitors was taken. Here, the total capacitance model

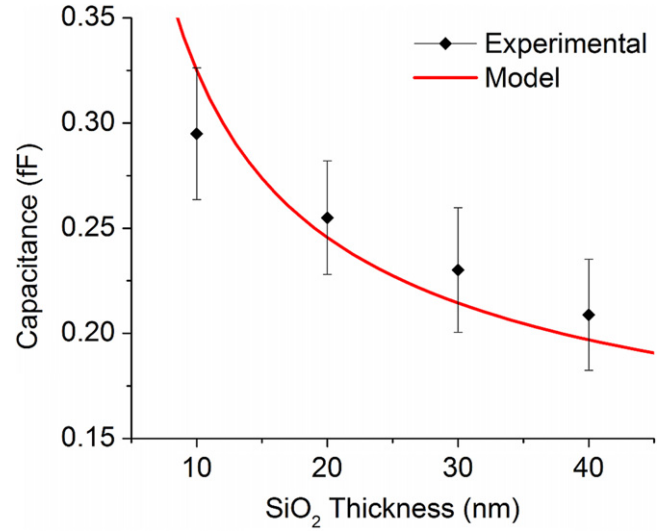


**Figure 5.** Measured capacitance of each  $\text{SiO}_2$  step (black diamonds). Error bars represent measurement noise during scanning across each step. Data are fitted with a capacitance model with fringe capacitance across the  $\text{SiO}_2$  layer taken into account. The model assumption that the NW end facet radius is the electromagnetic radius shows good agreement with the measured data to within 10%.

is reduced to  $C_{\text{cant}}$  in parallel with  $C_{\text{tip}}$  and  $C_{\text{step}}$  in series.  $C_{\text{tip}}$  is once again modeled as a simple parallel-plate capacitor and retains the same value from the model presented above.  $C_{\text{step}}$ , however, must account for fringing effects, as the ratio of the parallel-plate radius (tip radius)  $R$  to half the dielectric  $\text{SiO}_2$  thickness  $d$  ranges from 6–12. Fringe capacitance for a parallel plate capacitor is dependent upon a dimension characteristic of the width of the electrode, such as the disc diameter. The Kirchhoff–Hutson expression was derived as a first-order approximation for calculating total capacitance, however, its error increases for small  $R/d$  values. As such, an improved empirical equation incorporating higher order terms into the Kirchhoff–Hutson expression, with error <1% when compared to numerical simulations, was used [40]:

$$\frac{C_{\text{diel}}}{C_{\text{elem}}} \approx 1 + \frac{2d}{\pi R} \ln \frac{8\pi R}{ed} + \left( \frac{d}{\pi R} \ln \frac{d}{8\pi R} \right)^2;$$

$$C_{\text{tot}} = \left[ \frac{1}{C_{\text{tip}}} + \frac{1}{C_{\text{diel}}} \right]^{-1} + C_{\text{cant}},$$

where  $C_{\text{elem}}$  is the parallel-plate model,  $d$  is half the  $\text{SiO}_2$  thickness,  $e$  is the permittivity of free space, and  $R$  is the NW radius. From figure 5, it can be seen that the  $\text{SiO}_2$  steps are at the measurement threshold for the W-ALD NW probe, because 10 nm changes in  $\text{SiO}_2$  thickness correspond to a  $\sim 0.03$  fF change in capacitance, with measurement noise for each step also corresponding to  $\sim 0.03$  fF.  $C_{\text{cant}}$  was determined by measuring  $|S_{11}|$  as a function of tip-sample separation with a  $2 \mu\text{m}$  approach curve. By this method, the stray capacitance contribution of  $C_{\text{cant}}$  was found from a linear relation to be  $0.6 \pm 0.04 \text{ aF nm}^{-1}$ , indicating that each 10 nm increase in topography due to the  $\text{SiO}_2$  staircase results in a  $\sim 6$  aF decrease in  $C_{\text{cant}}$ . Because this contribution is

approximately one order of magnitude smaller than the measurement resolution of our system,  $C_{\text{cant}}$  was once again determined to be negligible and omitted from the model. Using the same value of  $\alpha=0.5 \text{ fF}/\Delta\text{dBm}$  previously calculated, the model provides a reliable first-order approximation for the  $\text{SiO}_2$  steps across the thicknesses measured and agrees with the experimental data to within 10%, as shown in figure 5. Improvements can be further made to the fit by decreasing the value of  $C_{\text{tip}}$ . This is attributed to the likely case where the NW end facet is not flush with the sample during scanning, resulting in a reduced contact area and an increased effective dielectric thickness.

## Imaging 2D $\text{MoS}_2$ sheets

To further assess the performance of the W-ALD NW probe, we compared its topographical and microwave resolution against that of a commonly used commercial Pt NSMM probe (4.5 kHz Rocky Mountain Nanotechnology 12Pt400A) (see footnote 3). We chose a  $\text{MoS}_2$  sample for imaging measurements due to its potential applications in CMOS-like logic devices and as a transparent semiconductor in photovoltaic and other optoelectronic structures [41, 42].  $\text{MoS}_2$  is a member of the layered transition-metal dichalcogenide materials with crystals composed of vertically stacked layers held together by van der Waals forces. Unlike pure graphene,

single layer  $\text{MoS}_2$  is a direct bandgap semiconductor (1.8 eV) and therefore a candidate for replacing Si in transistor designs without the need for increased fabrication complexity. One–four-layer-thick  $\text{MoS}_2$  was extracted from a bulk sample by use of the Scotch Tape method and then deposited on 260 nm of  $\text{SiO}_2$  grown on a p-type Si wafer [43]. Both probes were scanned over the same  $\text{MoS}_2$  patch at  $\sim 2.3 \text{ GHz}$  and with a scan area of  $10 \mu\text{m} \times 10 \mu\text{m}$ . Figure 6(a) shows the topographical results for the W-ALD NW probe. The different layers (each  $6.5 \text{ \AA}$  thick) are clearly visible with sheet edges well defined. By comparison, in figure 6(d), the topographical results for the Pt probe are shown, and the sheet edges are no longer sharp, while the single-layer region is poorly resolved. In figures 6(b) and (c), the amplitude and phase components of the microwave reflection  $S_{11}$  are shown for the W-ALD NW probe. Both single and multilayer  $\text{MoS}_2$  sheets are clearly visible in the  $S_{11}$  amplitude and phase images. The dashed white oval highlights the transition from one- to two-layer  $\text{MoS}_2$ , which can be seen in all three W-ALD NW image modes. The physics underlying the microwave contrast in the  $\text{MoS}_2$  sample will be explored in depth in an upcoming publication. Figures 6(e) and (f) show the amplitude and phase results respectively for the Pt tip. These images are set to the same intensity scale as the W-ALD NW results, allowing for a direct comparison between the image contrasts. Although it maintains good multilayer edge resolution, phase contrast is reduced with a loss of sensitivity to

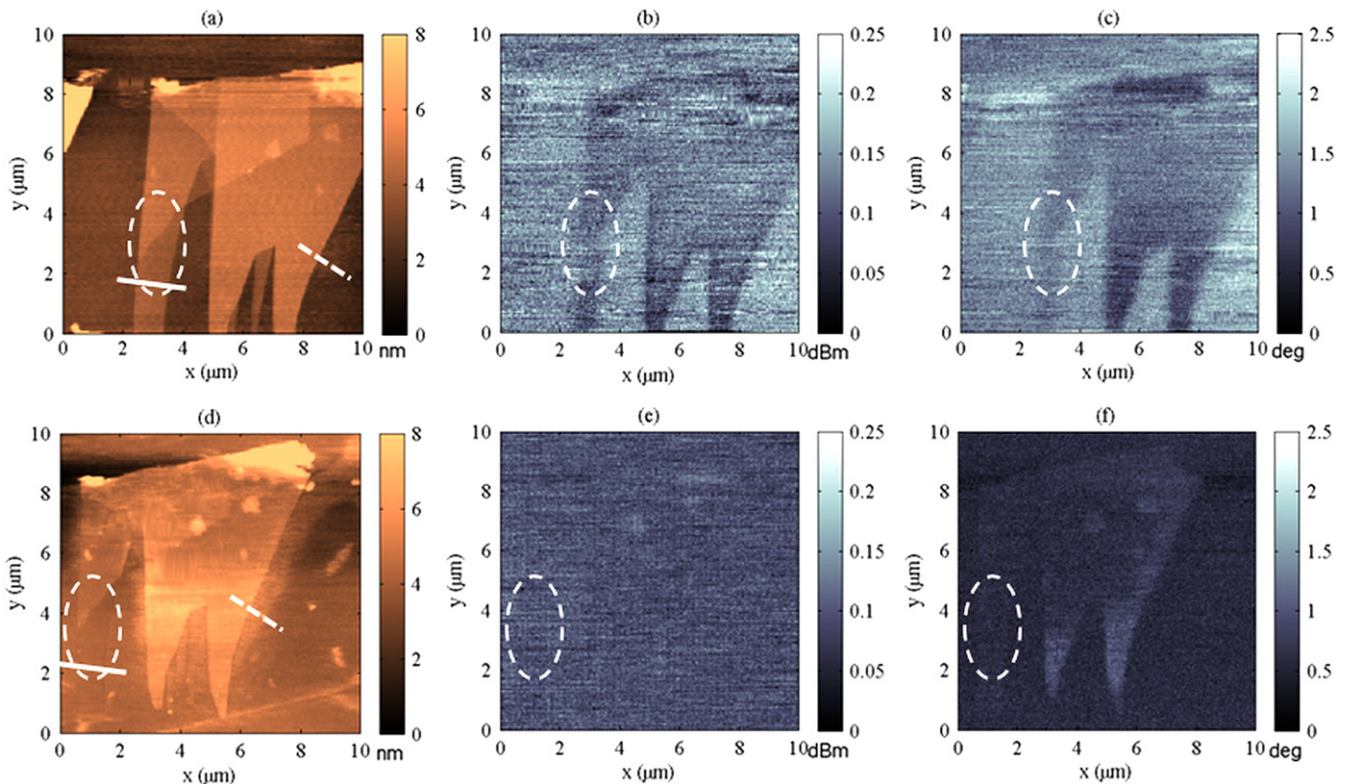


**Figure 6.** (a) Topography of the  $\text{MoS}_2$  sample with the W-ALD NW probe showing high edge definition. Solid and dashed white lines indicate, respectively, location of single-layer and multilayer line cuts for figure 7. (b) and (c)  $|S_{11}|$  amplitude and phase, respectively, with the W-ALD NW probe with sensitivity to the one- to two-layer  $\text{MoS}_2$  transition (dashed white oval). (d) Topography result from the commercial Pt probe showing reduced edge definition and lack of sensitivity to the single-layer region. (e) and (f)  $|S_{11}|$  amplitude and phase, respectively, from the commercial Pt probe with only minimal contrast present in the phase image. All images were taken with the same normal force of a few nanonewtons.

the single-layer MoS<sub>2</sub> sheet. Furthermore, amplitude sensitivity is almost completely eliminated in the case of the Pt tip, with measurement noise dominating the scan.

The MoS<sub>2</sub> sample was further examined in an effort to determine the cause of varying resolution between the two probes. For the above data, the MoS<sub>2</sub> was imaged first by the commercial Pt probe (with the result shown in figure 6(d)) before being scanned by the W-ALD NW probe (figure 6(a)). Figure 7(a) shows a follow-up topography scan with the Pt probe showcasing improved edge definition and single-layer contrast. Line cuts of 2.5  $\mu\text{m}$  across the single-layer region (solid white line) and across the multilayer-SiO<sub>2</sub> region (dashed white line) were taken from the same area for each of the three topography scans. The results are shown in figures 7(b) and (c), respectively. In figure 7(b), the top-line scan (black) represents the first Pt probe result which exhibits no obvious topographical sensitivity to the single layer region. The middle-line scan (red) represents the W-ALD NW probe, and here the single-layer region is clearly shown with a lateral resolution of  $\sim 100$  nm for the 6.5  $\text{\AA}$  step. The bottom-line scan (blue) represents the final Pt probe scan. Sensitivity to the single-layer region is now improved with a lateral resolution of  $\sim 400$  nm. In figure 7(c), the line cuts produce a similar trend across the multilayer region. The W-ALD NW probe once again yields the cleanest edge definition followed by the second of the two Pt probe scans.

These line cuts indicate that the MoS<sub>2</sub> sheets may have a glue residue from the Scotch Tape on their surface. During scanning with the Pt probe, such a residue would result in a convolution between the topographical amplitude and phase as the cantilever rotates out of plane, subsequently reducing sensitivity to the MoS<sub>2</sub> edge boundaries. Because these scanning artifacts are reduced after the W-ALD NW probe imaging, we propose that the improvement in sensitivity observed with the commercial probe may be attributed to ‘cleaning’ of the sample surface through the removal of portions of the glue residue. It is important to note that the sample was first scanned with the Pt tip ten times with no apparent change in topography (figure 6(d)), while the first scan with the W-ALD NW probe yielded the resolution shown in figure 6(a). This indicates that the Pt probe performed negligible cleaning, if any, of the sample over the course of repeated scanning. Furthermore, the W-ALD NW probe still exhibits the highest contrast relative to either Pt probe result with a lateral resolution on the order of its tip radius, indicating that its flexible, high-aspect-ratio structure is possibly immune to any remaining glue residue, while providing a stable, uniform tip geometry that enables enhanced microwave contrast.

## Conclusion

In conclusion, we report on the fabrication of a GaN NW NSMM probe with a W-ALD microwave pathway. Scanning over a microcapacitor calibration sample has shown the probe to exhibit capacitance resolution on the order of 0.03 fF. Capacitance circuit models were developed to fit trends in

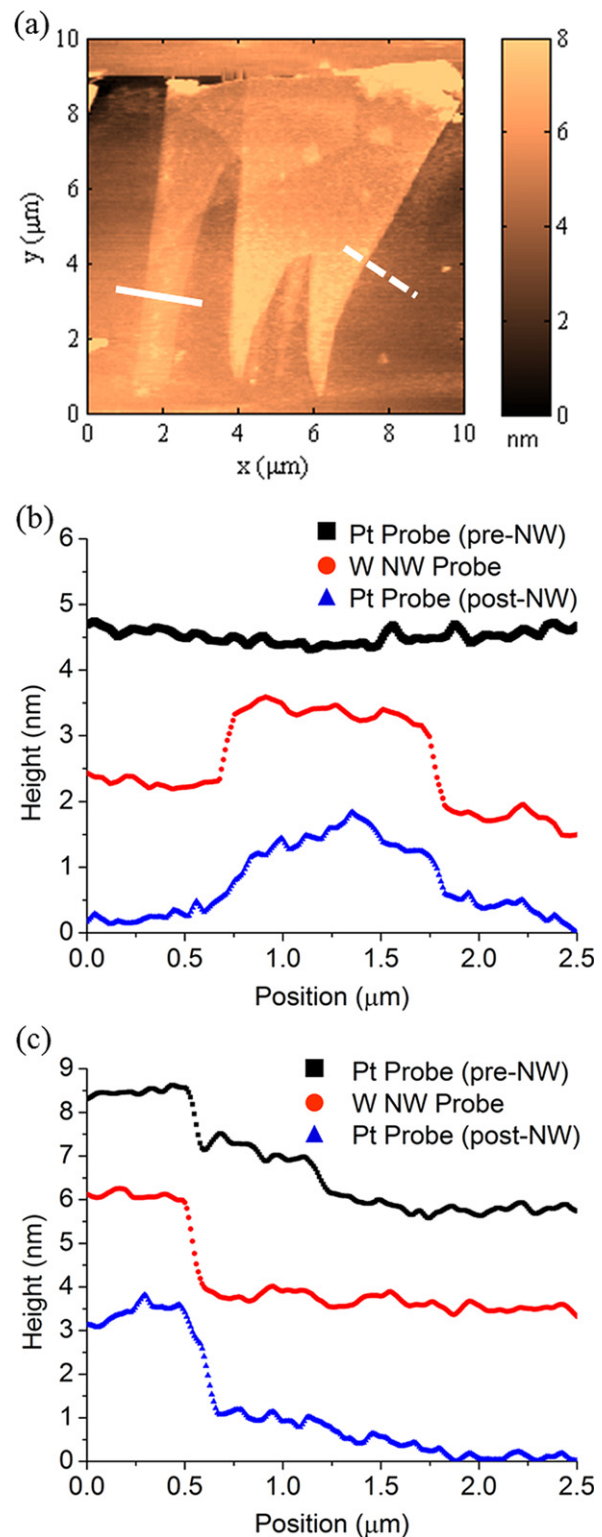


**Figure 7.** (a) Topography image from the commercial Pt probe after the W-ALD NW scan. Line cuts of 2.5  $\mu\text{m}$  are taken across the single-layer region (solid white line) and the multilayer region (dashed white line). (b) and (c) Results from single-layer and multilayer regions, respectively, with the top black line representing the Pt probe topography data before the W-ALD NW probe scan, the red line representing the W-ALD NW probe, and the blue line representing the Pt probe after the W-ALD NW probe scan. The latter Pt probe line cuts reveal an improved sensitivity to the MoS<sub>2</sub> edge, possibly owing to a reduction in the presence of glue residue. Note: line scans have been offset along the y-axis for viewing clarity.

changing microcapacitor area and dielectric thickness as well as tip interaction with the SiO<sub>2</sub> staircase with agreement to within 10%. Improvements can be made through a better understanding of both fringing fields through the dielectric thin films as well as possible bending of the NW structure and end facet during contact mode scanning. The W-ALD NW probe was shown to yield improved topographical and microwave sensitivity relative to a commercial Pt probe on 2D MoS<sub>2</sub> films, potentially due to its insensitivity to sample contamination in the form of glue residue. Future work will seek to enable the wafer-scale fabrication of NW probes through the incorporation of selective GaN NW growth into a clean-room process flow. The success of ALD as a thin, uniform electrical pathway also opens the possibility of creating a conductor/insulator device structure, thus enabling the formation of a shielded microwave pathway along the entire length of the cantilever.

## Acknowledgement

We thank Tasshi Dennis and Jason Gray for their critical reading of the manuscript.

## References

- [1] Anlage S M, Talanov V V and Schwartz A R 2006 Principles of near-field microwave microscopy *Scanning Probe Microscopy: Electrical and Electromechanical Phenomena at the Nanoscale* ed S V Kalinin and A Gruverman (New York: Springer-Verlag) pp 207–45
- [2] Hafner J H, Cheung C L and Lieber C M 1999 *Nature* **398** 761–2
- [3] Dai H, Hafner J H, Rinzler A G, Colbert D T and Smalley R E 1996 *Nature* **384** 147–50
- [4] Stadler J, Schmid T and Zenobi R 2012 *Nano Lett.* **12** 4514
- [5] Flöhr K, Sladek K, Günel H Y, Lepsa M I, Hardtdegen H, Liebmann M, Schäpers T and Morgenstern M 2012 *Appl. Phys. Lett.* **101** 243101
- [6] Kalkbrenner T, Ramstein M, Mlynek J and Sandoghdar V 2001 *J. Microsc.* **202** 72–6
- [7] Burt D P, Wilson N R, Weaver J M, Dobson P S and Macpherson J V 2005 *Nano Lett.* **5** 639–43
- [8] Tabib-Azar M and Wang Y 2004 *IEEE Trans. Microw. Theory Tech.* **52** 971–9
- [9] Gao C and Xiang X D 1998 *Rev. Sci. Instrum.* **69** 3846–51
- [10] Zhang L, Ju Y, Hosoi A and Fujimoto A 2010 *Rev. Sci. Instrum.* **81** 123708
- [11] Farina M, Mencarelli D, Di Donato A, Venanzoni G and Morini A 2011 *IEEE Trans. Microw. Theory Tech.* **59** 2769–76
- [12] Tselev A, Lavrik N V, Vlassiuk I, Briggs D P, Rutgers M, Proksch R and Kalinin S V 2012 *Nanotechnology* **23** 385706
- [13] Hung L T, Phuoc N N, Wang X-C and Ong C 2011 *Rev. Sci. Instrum.* **82** 084701
- [14] Plassard C, Bourillot E, Rossignol J, Lacroute Y, Lepleux E, Pacheco L and Lesniewska E 2011 *Phys. Rev. B* **83** 121409
- [15] Chiang C-J, Wallis T M, Gu D, Imtiaz A, Kabos P, Blanchard P T, Bertness K A, Sanford N A, Kim K and Filipovic D 2010 *J. Appl. Phys.* **107** 124301
- [16] Wallis T M, Gu D, Imtiaz A, Smith C S, Chiang C-J, Kabos P, Blanchard P T, Sanford N A and Bertness K A 2011 *IEEE Trans. Nanotechnol.* **10** 832–8
- [17] Budka T P, Waclawik S D and Rebeiz G M 1996 *IEEE Trans. Microw. Theory Tech.* **44** 2174–84
- [18] Tabib-Azar M, Su D P, Pohar A, LeClair S and Ponchak G 1999 *Rev. Sci. Instrum.* **70** 1725–9
- [19] Imtiaz A, Anlage S M, Barry J D and Melngailis J 2007 *Appl. Phys. Lett.* **90** 143106
- [20] Kim J, Babajanyan A, Sargsyan T, Melikyan H, Kim S, Friedman B and Lee K 2009 *Ultramicroscopy* **109** 958–62
- [21] Gramse G, Kasper M, Fumagalli L, Gomila G, Hinterdorfer P and Kienberger F 2014 *Nanotechnology* **25** 145703
- [22] Huber H P, Moertelmaier M, Wallis T M, Chiang C J, Hochleitner M, Imtiaz A, Oh Y J, Schilcher K, Dieudonne M and Smoliner J 2010 *Rev. Sci. Instrum.* **81** 113701
- [23] Huber H P, Humer I, Hochleitner M, Fenner M, Moertelmaier M, Rankl C, Imtiaz A, Wallis T M, Tanbakuchi H and Hinterdorfer P 2012 *J. Appl. Phys.* **111** 014301
- [24] Gao C, Wei T, Duetter F, Lu Y and Xiang X-D 1997 *Appl. Phys. Lett.* **71** 1872–4
- [25] Vlahacos C, Steinhauer D, Dutta S, Feenstra B, Anlage S M and Wellstood F 1998 *Appl. Phys. Lett.* **72** 1778–80
- [26] Karbassi A, Ruf D, Bettermann A, Paulson C, van der Weide D W, Tanbakuchi H and Stancliff R 2008 *Rev. Sci. Instrum.* **79** 094706
- [27] Wu S and Yu J-J 2010 *Appl. Phys. Lett.* **97** 202902
- [28] Gomila G, Toset J and Fumagalli L 2008 *J. Appl. Phys.* **104** 024315
- [29] Lányi Š 2005 *Ultramicroscopy* **103** 221–8
- [30] Weber J, Blanchard P, Sanders A, Imtiaz A, Wallis T, Coakley K, Bertness K, Kabos P, Sanford N and Bright V 2014 *Appl. Phys. Lett.* **104** 023113
- [31] Imtiaz A, Wallis T M, Lim S H, Tanbakuchi H, Huber H P, Hornung A, Hinterdorfer P, Smoliner J, Kienberger F and Kabos P 2012 *J. Appl. Phys.* **111** 093727
- [32] Bertness K A, Sanford N A and Davydov A V 2011 *IEEE J. Sel. Top. Quantum Electron.* **17** 847–58
- [33] Bertness K, Roshko A, Sanford N, Barker J and Davydov A 2006 *J. Cryst. Growth* **287** 522–7
- [34] Bertness K A, Roshko A, Mansfield L M, Harvey T E and Sanford N A 2007 *J. Cryst. Growth* **300** 94–9
- [35] Fabreguette F, Sechrist Z, Elam J and George S 2005 *Thin Solid Films* **488** 103–10
- [36] George S M 2009 *Chem. Rev.* **110** 111–31
- [37] Klaus J, Ferro S and George S 2000 *Thin Solid Films* **360** 145–53
- [38] Rosnagel S, Noyan I and Cabral C Jr 2002 *J. Vac. Sci. Technol. B* **20** 2047–51
- [39] Jain A, Ong S P, Hautier G, Chen W, Richards W D, Dacek S, Cholia S, Gunter D, Skinner D and Ceder G 2013 *APL Mater.* **1** 011002
- [40] Sloggett G, Barton N and Spencer S 1986 *J. Phys. A: Math. Gen.* **1** 2725
- [41] Radisavljevic B, Radenovic A, Brivio J, Giacometti V and Kis A 2011 *Nat. Nanotechnology* **6** 147–50
- [42] Mak K F, Lee C, Hone J, Shan J and Heinz T F 2010 *Phys. Rev. Lett.* **105** 136805
- [43] Novoselov K S, Geim A K, Morozov S, Jiang D, Zhang Y, Dubonos S, Grigorieva I and Firsov A 2004 *Science* **306** 666–9